Available online at www.sciencedirect.com

ScienceDirect

Green Energy & Environment 5 (2020) 473–483

www.keaipublishing.com/gee

Research paper

Engineering three-layer core–shell S-1/TS-1@dendritic-SiO_2 supported Au catalysts towards improved performance for propene epoxidation with H_2 and O_2

Zhaoning Song [a], Juncong Yuan [a], Zhenping Cai [b], Dong Lin [a], Xiang Feng [a,*], Nan Sheng [c], Yibin Liu [a], Xiaobo Chen [a], Xin Jin [a], De Chen [b], Chaohe Yang [a,*]

[a] *State Key Laboratory of Heavy Oil Processing, China University of Petroleum, Qingdao, 266580, China*
[b] *Department of Chemical Engineering, Norwegian University of Science and Technology, Trondheim, 7491, Norway*
[c] *State Key Laboratory of Safety and Control for Chemicals, SINOPEC Qingdao Research Institute of Safety Engineering, 218 Yanansan Road, Qingdao, 266580, China*

Received 12 July 2020; revised 22 October 2020; accepted 18 November 2020
Available online 22 November 2020

Abstract

The advocacy of green chemical industry has led to the development of highly efficient catalysts for direct gas-phase propene epoxidation with green, sustainable and simple essence. The S-1/TS-1@dendritic-SiO_2 material with three-layer core–shell structure was developed and used as the support for Au catalysts, which showed simultaneously fantastic PO formation rate, PO selectivity and stability (over 100 h) for propene epoxidation with H_2 and O_2. It is found that silicalite-1 (S-1) core and the middle thin layer of TS-1 offer great mass transfer ability, which could be responsible for the excellent stability. The designed dendritic SiO_2 shell covers part of the acid sites on the external surface of TS-1, inhibiting the side reactions and improving the PO selectivity. Furthermore, three kinds of SiO_2 shell morphologies (i.e., dendritic, net, mesoporous shell) were designed, and relationship between shell morphology and catalytic performance was elucidated. The results in this paper harbour tremendous guiding significance for the design of highly efficient epoxidation catalysts.

Keywords: Propene epoxidation; Selectivity; Core-shell; Dendritic SiO_2 shell; TS-1

1. Introduction

Propylene epoxide (PO) is one of the indispensable chemical intermediates for the production of bulk chemicals such as polyether polyols and propylene glycol [1]. Currently, PO is mainly manufactured through chlorohydrin process, organic peroxide processes and HPPO process in industry [2–5]. However, the environmental issues, complexity and low profit accompanied by the above processes are urgently calling for more efficient processes to produce PO.

To date, researchers have tried to catalyze propene epoxidation with O_2 over Ag-based catalysts in the similar way to ethylene epoxidation. However, the allyl hydrogen in propene is easier to be oxidized, leading to very low selectivity of PO over Ag-based catalysts [6,7]. In 1998, Haruta and co-workers found that anatase titanium dioxide can be used as support for Au-based catalysts for propene epoxidation with H_2 and O_2, which showed high PO selectivity ($\geq$ 90%) [8]. This process has attracted worldwide attention from both academia and industry. Therefore, various titanium-containing supports have

* Corresponding authors.
E-mail addresses: xiangfeng@upc.edu.cn (X. Feng), yangch@upc.edu.cn (C. Yang).

https://doi.org/10.1016/j.gee.2020.11.017

been investigated to improve the catalytic performance [9–12]. Especially, Au/titanium silicate-1 (Au/TS-1) displayed good C_3H_6 conversion (> 5.0%) and PO selectivity (> 90%) at 200 °C [13,14]. Nevertheless, it also exhibited poor stability and deactivated rapidly within several hours [2,15–19]. According to our previous works [20–23], the narrow micropores of TS-1 are easy to generate carbonaceous deposits, resulting in the micropore blocking deactivation. Additionally, improving the mass transfer ability and surface hydrophobicity of TS-1 have been confirmed to be key strategies for solving the rapid deactivation problem [21–24]. Considering this, we developed a core–shell S-1/TS-1 support with TS-1 shell and silicalite-1 (S-1) core, which showed unique stability during 100 h. However, the performance can be further boosted in order to accelerate the promising industrialization process [25].

In this work, a S-1/TS-1@dendritic-SiO_2 with three-layer structure was designed as support for Au catalysts to achieve the simultaneously excellent catalytic stability (over 100 h), PO selectivity (93.9%), PO formation rate (143.4 $g_{PO}h^{-1}$ $kg_{TS\text{-}1}{}^{-1}$) and H_2 efficiency (26.1%). Moreover, the intrinsic structure–performance relationship between the multifunctional Au/S-1/TS-1@dendritic-SiO_2 catalyst and catalytic performance is well elucidated. It is found that internal S-1/TS-1 structure offer great mass transfer ability, which is responsible for the high stability. In addition, an external SiO_2 inert shell can cover part of the Lewis acid sites provided by $Ti(OSi)_3OH$, which could improve the selectivity by inhibiting the PO ring-opening. Moreover, with the change of SiO_2 shell morphologies (i.e., dendritic, net and mesoporous shell), the volcanic-shape relationship between shell density and PO formation rate was elucidated. This study will be of great importance to the design of highly efficient supported Au/Ti-based catalysts for direct propene epoxidation with H_2 and O_2.

2. Materials and methods

2.1. Materials

Tetraethyl orthosilicate (TEOS, 99%), titanium butoxide (TBOT, 99%), tetrapropylammonium hydroxide solution (TPAOH, 1M), *n*-butylamine (NBA, 99.5%), sodium hydroxide (NaOH, 98%), cetyltrimethylammonium bromide (CTAB, 99%), aqueous ammonia (NH_4OH, 25–28%) and ethanol (99.9%) were obtained from Aladdin Company. Ethyl ether (99.5%) and chloroauric acid ($HAuCl_4\cdot4H_2O$) were purchased from Sinopharm Chemical Reagent Company. All chemicals were analytical grade and used without further purification.

2.2. Synthesis of core–shell S-1/TS-1

The S-1/TS-1 was prepared by the method developed in our previous research [25]. The solution molar compositions are: SiO_2: TiO_2: TPAOH: *n*-butylamine: H_2O = 1.0: 0.024: 0.1: 0.4: 30. The S-1 seed (prepared according to the literature [26]) was added into the above solution and the mass ratio of S-1 seed to SiO_2 is 0.33. The final seriflux was poured into a Teflon-lined stainless-steel autoclave and crystallized for 72 h at 170 °C. After crystallization, the product solution was centrifuged and washed with distilled water for at least 3 times. The products were then dried at 100 °C for 12 h and calcined at 550 °C for 6 h.

2.3. Synthesis of three-layer core–shell S-1/TS-1@dendritic-SiO_2

1.0 g S-1/TS-1 powder was added to a solution composed of 1.5 g cetyltrimethylammonium bromide (CTAB), 210 mL H_2O, 30–160 mL ethanol, 2.4 mL aqueous ammonia and 0–60 mL ethyl ether. After 10 min of ultrasound and 30 min of stirring at 25 °C, 1.5 mL TEOS was added dropwise into the solution. The above solution was stirred for 6 h at 25 °C. The final seriflux was centrifuged, washed, dried at 100 °C for 12 h, and finally calcined at 550 °C for 6 h.

2.4. Au deposition

Au/S-1/TS-1@dendritic-SiO_2, Au/S-1/TS-1 and Au/TS-1 catalysts were prepared by the traditional deposition–precipitation procedure [15] as follows: 0.1 g $HAuCl_4\cdot4H_2O$ and 50 mL deionized water were mixed evenly at 25 °C. Then, 0.5 g support was added to the solution. The pH of the resulting solution was then adjusted the pH to 6.8–7.4 with NaOH solution and maintained for hours. Finally, the catalyst slurry was centrifuged, washed three times by 50 mL deionized water and dried for 12 h at 25 °C under vacuum.

2.5. Characterizations

The S-1/TS-1@dendritic-SiO_2 structure was tested by the X-ray diffraction patterns (XRD) on an X'pert PRO MPD diffractometer instrument using Cu-Kα radiation. The pore properties of the S-1/TS-1@dendritic-SiO_2 were measured by the N_2 adsorption–desorption on a Micromeritics ASAP 2020 instrument. The presence of Ti was determined by the fourier transform infrared spectroscopy (FT-IR) spectra on a Nicolet NEXUS 670 spectrometer with KBr as background. The Ti species were determined by the ultraviolet–visible spectroscopy (UV-vis) spectra on a PerkinElmer Lambda 35 spectrophotometer with $BaSO_4$ as background. The high-resolution transmission electron microscopy (HRTEM) images were taken on a JEOL JSM-2100F microscope, and the scanning electron microscopy (SEM) images were obtained on a Hitachi S-4800 field-emission scanning electron microscope. Over 120 Au nanoparticles were measured for their sizes to ascertain the average Au particle size in order to improve the precision. The Au loading and Ti content of Au/S-1/TS-1@dendritic-SiO_2 were detected by the inductive coupled plasma optical emission spectrometry (ICP-OES) on an Agilent 730 ICP-OES spectrometer. The surface Ti content was determined by the X-ray photoelectron spectroscopy (XPS) on a Perkin–Elmer PHI 5000C ESCA system. The surface acidity of S-1/TS-1@dendritic-SiO_2 was detected by Ammonia

temperature-programmed desorption (NH_3-TPD) on the Micromeritics AutoChem II 2920 instrument. To better compare the NH_3-TPD results, the amount of internal S-1/TS-1 in S-1/TS-1@dendritic-SiO_2 sample was kept the same to that of S-1/TS-1 sample. The type and concentration of acid sites of the samples were analyzed by pyridine adsorption Fourier-transform infrared (pyridine-IR) on a Bruker tensor 27 instrument. For pyridine adsorption, the wafer was cooled down to 298 K and saturated adsorbed by pyridine for 2 h. The pyridine-IR spectra of the wafers were tested at 298 K after desorption of pyridine at 423 K for 1 h under the dynamic vacuum (10.6–10.7 mbar).

2.6. Gas-phase propene epoxidation with H_2 and O_2

Gas-phase propene epoxidation reaction was taken in a quartz tubular reactor (i.d. 8 mm) employing 0.15 g catalysts with 80–100 mesh size. The reaction gases include C_3H_6, H_2, O_2 and N_2, with the flow rate of 3.5/3.5/3.5/24.5 mL min^{-1}, respectively. The space velocity was 14,000 mL h^{-1} $g_{Cat}{}^{-1}$. Catalysts were tested at 200 °C under atmospheric pressure. The reactants and products were analyzed using two on-line GC (Agilent 6890). Propylene oxide (PO) and other hydrocarbons can be analyzed by the GC equipped with FID. C_3H_6, H_2, O_2, N_2 and CO_2 were analyzed by GC equipped with TCD. The propene conversion, PO selectivity and H_2 efficiency can be calculated according to formulas Eqs. (1)–(3), respectively. The PO formation rate ($g_{PO}h^{-1}$ $kg_{TS\text{-}1}{}^{-1}$) is calculated according to the mass of TS-1 because only TS-1 is active towards PO formation. The mass of TS-1 is obtained by subtracting the mass of SiO_2 shell and S-1 core from the total mass of catalyst.

$$Propene\ conversion = \frac{mol\ of\ \left(C_3 - oxygenates + \frac{2}{3}ethanal + \frac{1}{3}CO_2\right)}{mol\ of\ propene\ in\ the\ feed} \quad (1)$$

$$PO\ selectivity = \frac{mol\ of\ PO}{mol\ of\ \left(C_3 - oxygenates + \frac{2}{3}ethanal + \frac{1}{3}CO_2\right)} \quad (2)$$

$$H_2\ efficiency = \frac{mol\ of\ PO}{mol\ of\ H_2\ converted} \quad (3)$$

3. Results and discussion

3.1. Three-layer core–shell S-1/TS-1@dendritic-SiO_2 structure

The physico-chemical properties of S-1/TS-1@dendritic-SiO_2 and traditional TS-1 (prepared by the procedure reported by Khomane [27]) with the same Si/Ti ratio are first compared. As can be seen in XRD patterns (Fig. 1a), both S-1/TS-1@dendritic-SiO_2 and traditional TS-1 possess the five diffraction peaks at 7.98°, 8.88°, 23.18°, 23.98° and 24.38°, coinciding with the MFI zeolitic topological structure [28] and showing a high crystallinity degree. The N_2 adsorption–desorption isotherms of both samples are displayed in Fig. 1b. For the TS-1, the rapid elevation of the curve at $P/P_0 < 0.02$ indicates the only existence of micropores [21]. For the S-1/TS-1@dendritic-SiO_2, the adsorption–desorption curves show the typical IUPAC type IV isotherms with a H3 hysteresis loop, which illustrates a very unique hierarchical structure.

The environment of titanium species in TS-1 can be verified by FT-IR and UV-vis spectra. In the FT-IR spectra (Fig. 1c), the S-1/TS-1@dendritic-SiO_2 sample exhibits six typical characteristic bands at 450, 550, 800, 960, 1100 and 1230 cm^{-1}, which are in accordance with the typical FT-IR spectra of TS-1 [23]. The adsorption bands at 450, 550, 800, 1100 and 1230 cm^{-1} are the characteristic absorption bands of MFI framework structure. The band at 960 cm^{-1} is considered to be the presence of the titanium species inside the framework. The UV-vis spectra of S-1/TS-1@dendritic-SiO_2 and traditional TS-1 samples are shown in Fig. 1d. It is obvious that the main adsorption peak at ca. 210 nm appears in both samples, implying the existence of the framework isolated Ti(IV) species [29,30] which are the key active sites for epoxidation reactions. Moreover, no obvious absorption peaks appear at 260 and 330 nm, indicating that neither sample contains octahedrally coordinated Ti complexes nor anatase TiO_2 species.

Additionally, the morphology and structure of S-1/TS-1@dendritic-SiO_2 were also analyzed by the SEM, TEM and TEM-Mapping images. It can be seen from Fig. 2a and b that the S-1/TS-1@dendritic-SiO_2 contains a core–shell structure with an intertwined dendritic mesoporous SiO_2 shell. Meanwhile, it can be clearly observed from Fig. 2c and d that the dendritic SiO_2 shell has open pores with a diameter of 5–100 nm. In the TEM-Mapping images (Fig. 2e), the three-layer core–shell structure of S-1/TS-1@dendritic-SiO_2 could be clearly observed. The complete structure of S-1/TS-1@dendritic-SiO_2 includes an intertwined dendritic mesoporous SiO_2 shell, a titanium-rich TS-1 intermediate layer and a silicon-rich S-1 core. Moreover, the distribution of Ti element (Fig. 2e) indicates that the thickness of the TS-1 layer is only about 90 nm, much smaller than that of traditional TS-1 (ca. 500 nm) in Fig. S1.

In order to further determine the distribution of Ti element of S-1/TS-1, the holistic Ti content and the surface Ti content were detected by the ICP-OES and XPS, respectively. The ICP-OES and XPS results illustrate that the surface Ti content of 1.01% is evidently higher than that of 0.80% of the holistic Ti content, indicating the S-1/TS-1 contains a core–shell structure with a titanium-rich shell. This is also confirmed by the TEM-Mapping images in Fig. 2e. This phenomenon could be related to the dissolution–recrystallization process of S-1 seeds during crystallization in alkaline environment [25].

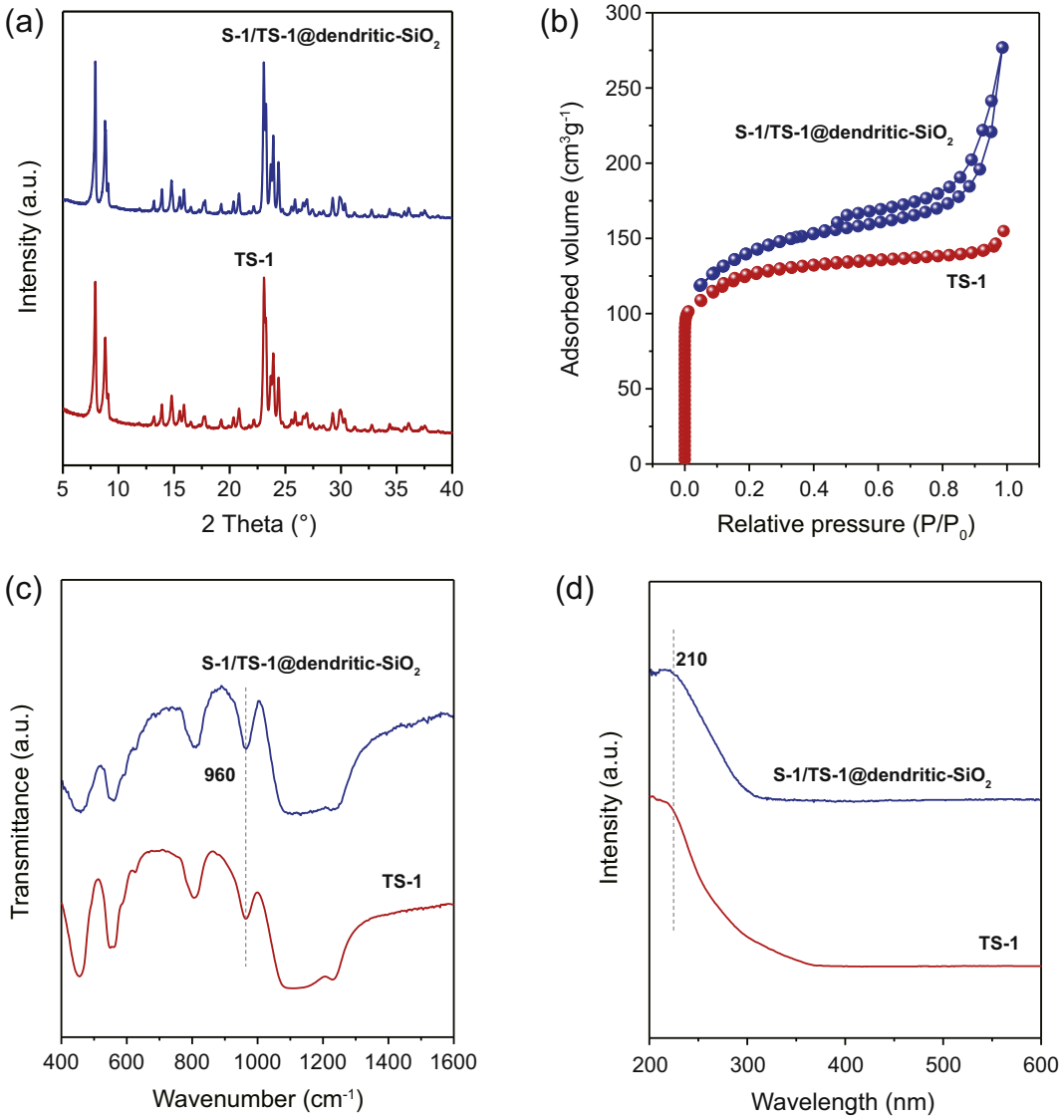

Fig. 1. XRD spectra (a), N_2 adsorption–desorption isotherms (b), FT-IR spectra (c) and UV-vis spectra (d) of S-1/TS-1@dendritic-SiO_2 and traditional TS-1.

3.2. Catalytic performance of Au/S-1/TS-1@dendritic-SiO_2

The S-1/TS-1@dendritic-SiO_2 was used as support for Au deposition, and compared with Au/S-1/TS-1 and traditional Au/TS-1 catalysts. The HRTEM images of the three catalysts with unified loading of 0.10 wt% are displayed in Fig. 3. It can be seen that all of them exhibit similar Au average particle size of ca. 3 nm. This result can exclude the influence of Au particle size on catalytic performance [31–34].

In addition, the Au NPs location of Au/S-1/TS-1@dendritic-SiO_2 is further investigated by TEM image in Fig. S2. The TEM image of Au/S-1/TS-1@dendritic-SiO_2 shows that most Au NPs are loaded on the TS-1 intermediate layer rather than on the SiO_2 shell. This is because when Au NPs are loaded by deposition–precipitation method, Au NPs are more likely to be loaded on the TS-1 intermediate layer (isoelectric point of 7) rather than on SiO_2 shell (isoelectric point of 2) at pH of 7 according to the isoelectric point principle [8]. The catalytic performance of the Au/S-1/TS-1@dendritic-SiO_2, Au/S-1/TS-1 and traditional Au/TS-1 catalysts for propene epoxidation with H_2 and O_2 are compared in Fig. 4. The traditional Au/TS-1 catalyst exhibits slightly higher initial PO formation rate of 156 $g_{PO}h^{-1}$ $kg_{TS\text{-}1}{}^{-1}$. Nevertheless, it can be found that the Au/TS-1 catalyst rapidly deactivated within 20 h, and the PO formation rate sharply dropped from 156 to 105 $g_{PO}h^{-1}$ $kg_{TS\text{-}1}{}^{-1}$. This is because of the microspores blocking caused by carbonaceous deposits, which inhibits the transfer of reactants and products in the microporous channels [20]. In contrast, the Au/S-1/TS-1 and Au/S-1/TS-1@dendritic-SiO_2 exhibit significantly improved stability (more than 100 h). The mechanism for the enhanced stability is mainly

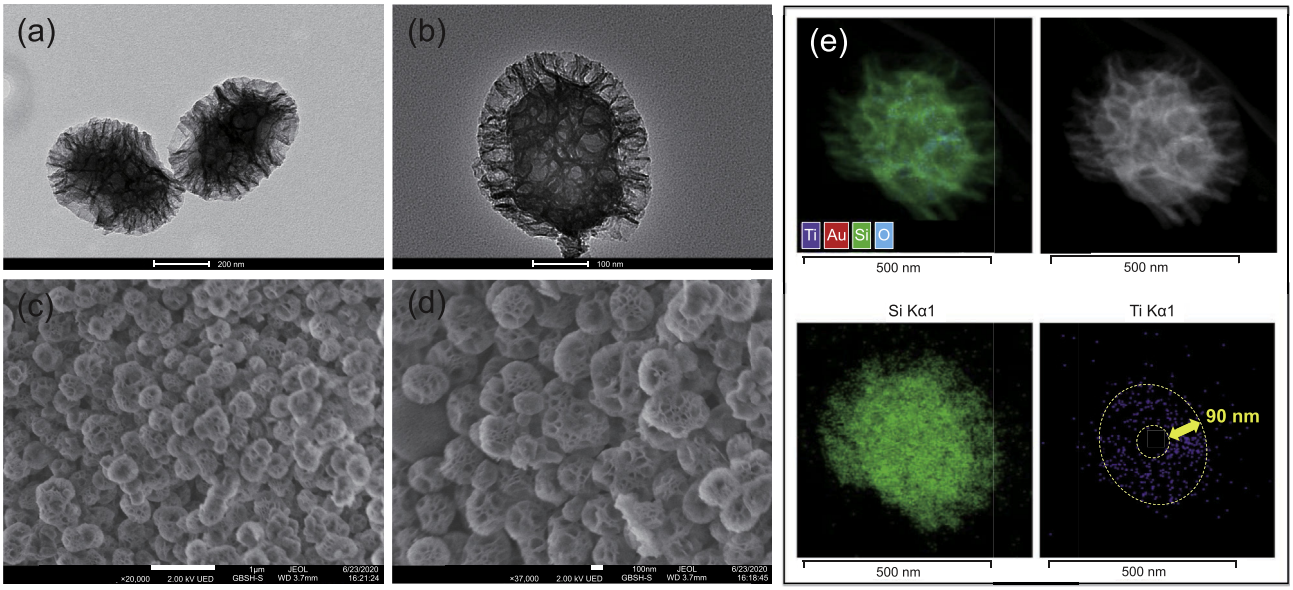

Fig. 2. TEM (a–b), SEM (c–d) and TEM-Mapping (e) images of S-1/TS-1@dendritic-SiO_2.

due to the unique S-1/TS-1 core–shell structure. As shown in Fig. S3, S-1/TS-1 contains a thin TS-1 layer (only 90 nm) and an S-1 core. During the Au loading process, the Au nanoparticles are mainly loaded on the TS-1 layer due to the unique deposition–precipitation mechanism [8]. Therefore, the reactions mainly occur on the Au–Ti sites in the thin TS-1 layer (only 90 nm) of the catalyst. The thin TS-1 layer of S-1/TS-1 core–shell structure makes the products more easily diffused out to the gas phase because of the shortened diffusion length in the catalyst [21]. In addition, when part of products penetrate S-1 core, the ring–opening reactions are inhibited possibly because S-1 has low ability to catalyze ring–opening reactions [35]. Furthermore, for Au/S-1/TS-1@dendritic-SiO_2, dendritic-SiO_2 shell also plays a key role in improving stability. The coated SiO_2 shell can shield the acidic sites, thereby avoiding the catalyst deactivation caused by the carbonaceous deposits from the by-products. At the same time, the pore structure of dendritic-SiO_2 shell facilitate the mass transfer of reactants and products. Therefore, coating dendritic-SiO_2 shell can further enhance the stability of the catalyst.

Notably, high PO selectivity (93.9%) is also observed for Au/S-1/TS-1@dendritic-SiO_2 catalyst. This is higher than that of Au/S-1/TS-1 catalyst (87.3%). The by-products such as CO_2 and ethanal produced by ring–opening reaction are reduced. It is reported that the surface acid sites originating from defective Ti–OH species can trigger side reactions such as ring–opening reaction of PO [36–40]. Therefore, the high PO selectivity of Au/S-1/TS-1@dendritic-SiO_2 may be attributed to the coverage of surface acid sites by the inert SiO_2 shell. However, the coverage of surface acid sites by the inert SiO_2 shell may also results in the slight decline of C_3H_6 conversion (4.18%). Nevertheless, due to the impressive PO selectivity, the PO formation rate of Au/S-1/TS-1@dendritic-SiO_2 (143.4 $g_{PO}h^{-1}$ $kg_{TS\text{-}1}{}^{-1}$) is higher than that of Au/S-1/TS-1 (140.9 $g_{PO}h^{-1}$ $kg_{TS\text{-}1}{}^{-1}$). Moreover, it is noteworthy in Fig. 4b that the H_2 efficiency of Au/S-1/TS-1@dendritic-SiO_2 (26.1%) is higher than that of Au/TS-1 (22.5%) and Au/S-1/TS-1 (21.9%). The H_2 efficiency for this reaction is closely relevant to the formation and decomposition of H_2O_2. Since the H_2O_2 is easily decomposed on the acid sites at reaction temperature of 200 °C, covering the acid sites can alleviate the decomposition of H_2O_2 and consequently increase the H_2 efficiency.

In order to further verify the effects of the coated dendritic SiO_2 shell on the acid sites of the S-1/TS-1 zeolite, NH_3-TPD of dendritic SiO_2, S-1/TS-1 and S-1/TS-1@dendritic-SiO_2 were performed. Firstly, as can be seen from Fig. 5 that only one extremely weak NH_3 desorption peak of dendritic SiO_2 appears at 262 °C, revealing that a very small number of weak acid centers exist in SiO_2. Therefore, it can be considered that the influence of the acidity by SiO_2 is negligible. By contrast, both S-1/TS-1 and S-1/TS-1@dendritic-SiO_2 exhibit two obvious NH_3 desorption peaks at 139 and 327 °C, which are ascribed to weak acid centers. It is known that the overmuch acid sites provided by defective Ti–OH on TS-1 zeolite can reduce the PO selectivity by the ring–opening reactions of PO [36,39,40]. Notably, the peaks of S-1/TS-1@dendritic-SiO_2 are much weaker than those of S-1/TS-1, indicating that coating the dendritic-SiO_2 shell remarkably decrease the number of Lewis acid sites.

Furthermore, the acid sites (i.e. the defective Ti–OH) contents were also determined by UV-vis spectra (Fig. 6).

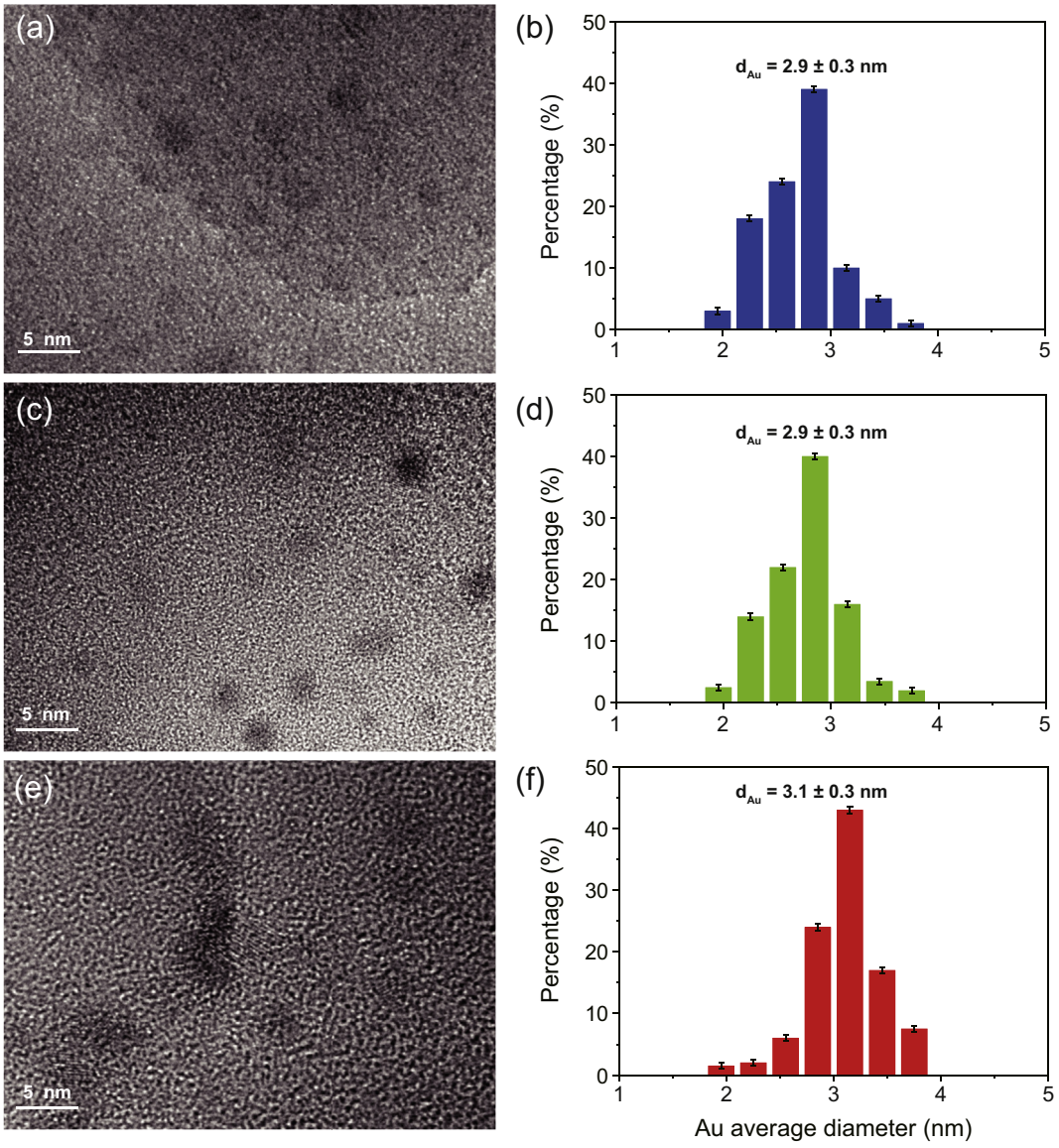

Fig. 3. HRTEM images and corresponding Au particle size distributions of Au/S-1/TS-1@dendritic-SiO_2 (a, b), Au/S-1/TS-1 (c, d) and traditional Au/TS-1 (e, f) catalysts.

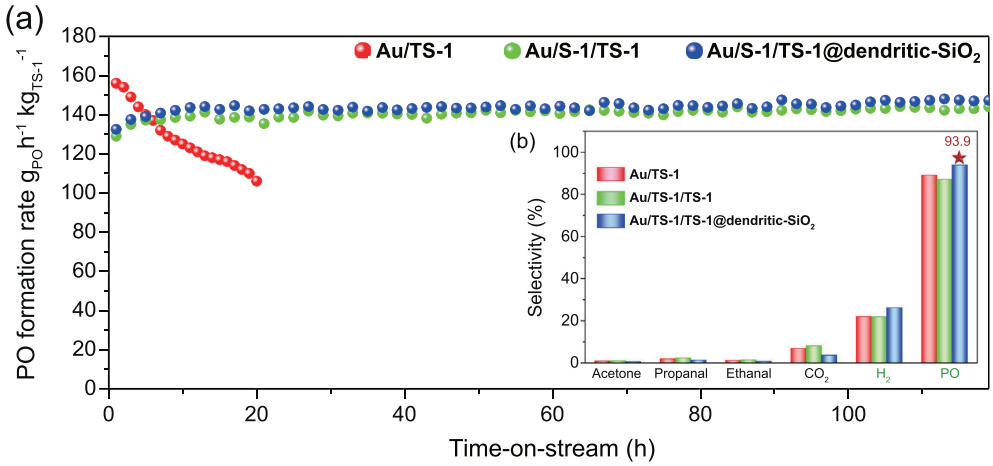

Fig. 4. PO formation rate (a) and detailed products selectivities (b) of Au/S-1/TS-1@dendritic-SiO_2, Au/S-1/TS-1 and traditional Au/TS-1 catalysts at different time-on-stream.

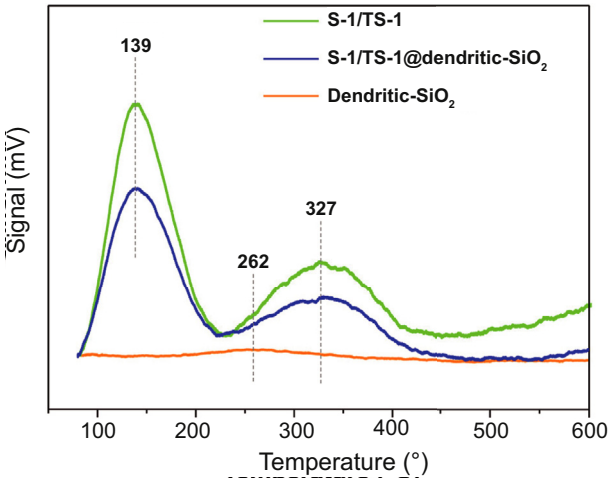

Fig. 5. NH_3-TPD spectra of dendritic SiO_2, S-1/TS-1 and S-1/TS-1@dendritic-SiO_2.

The peak at 235 nm can be ascribed to the open site Ti(O-Si)$_3$OH species that provide acid sites [41,42], whereas the peak at 210 nm can be ascribed to the close site Ti(OSi)$_4$ species. Therefore, the normalized area ratio ($A_{235\ nm}/A_{210\ nm}$) can be used as a descriptor to reflect the acid content. It is calculated from Fig. 6a that the $A_{235\ nm}/A_{210\ nm}$ for S-1/TS-1 is 0.75, which is higher than that of S-1/TS-1@dendritic-SiO_2 (0.58), indicating that there are less surface acid sites for S-1/TS-1@dendritic-SiO_2 due to dendritic-SiO_2 coating. This result is in consistent with the above NH_3-TPD spectra (Fig. 5). The decline of surface acid sites content can inhibit side reactions such as PO ring-opening, thus improving the PO selectivity.

3.3. The relationship between SiO_2 shell morphology and catalytic performance

Based on the above results, the SiO_2 shell is beneficial to the improvement of PO selectivity and H_2 efficiency. Herein, we further investigated the influence of the SiO_2 shell morphology on the catalyst performance. Three kinds of SiO_2 shells with different morphologies were prepared by adjusting the feeding amount of ether, i.e. S-1/TS-1@dendritic-SiO_2, S-1/TS-1@net-SiO_2 and S-1/TS-1@meso-SiO_2 with the corresponding ether amount of 60 mL, 40 mL and 0 mL, respectively. The formation of dendritic and net structure of SiO_2 results from the gasification of ethyl ether in the exothermic hydrolysis and condensation of TEOS [43]. As shown in Fig. 7, the thickness of SiO_2 shell in the three samples is in a similar range of 70–75 nm. This can exclude the influence of the SiO_2 shell thickness on catalytic performance [19]. Meanwhile, with the decrease of the ether feeding amount, the density of dendritic structure progressively increases. The dendritic structure finally evolves into an ordered mesoporous structure. Meanwhile, the core–shell structure diagrams of the three samples are shown in Fig. 7c, f, i.

The N_2 adsorption–desorption isotherms and pore-size distribution of S-1/TS-1@dendritic-SiO_2, S-1/TS-1@net-SiO_2 and S-1/TS-1@meso-SiO_2 are shown in Fig. S4 and Table 1. It can be seen in Fig. S4a–c that the N_2 adsorption–desorption isotherms of the three samples are all type IV isotherms according to IUPAC's classification, indicating the meso-structured materials. With respect to the pore size distribution in Fig. S4d–f, all three samples have the mesoporous size of ca. 2.4 nm. Meanwhile, wide peaks with mesoporous

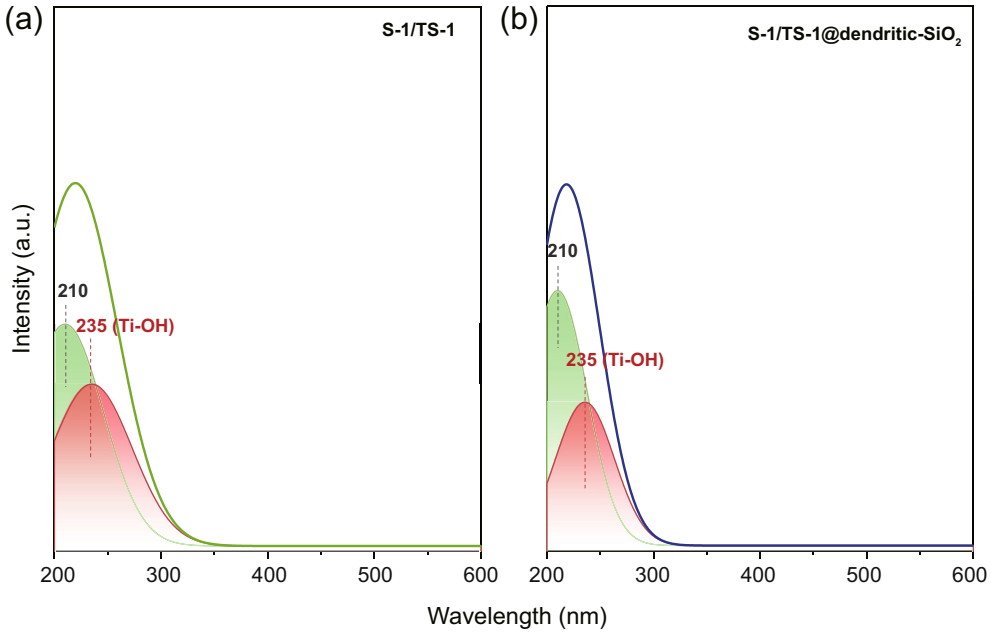

Fig. 6. UV-vis spectra of S-1/TS-1 (a) and S-1/TS-1@dendritic-SiO_2 (b).

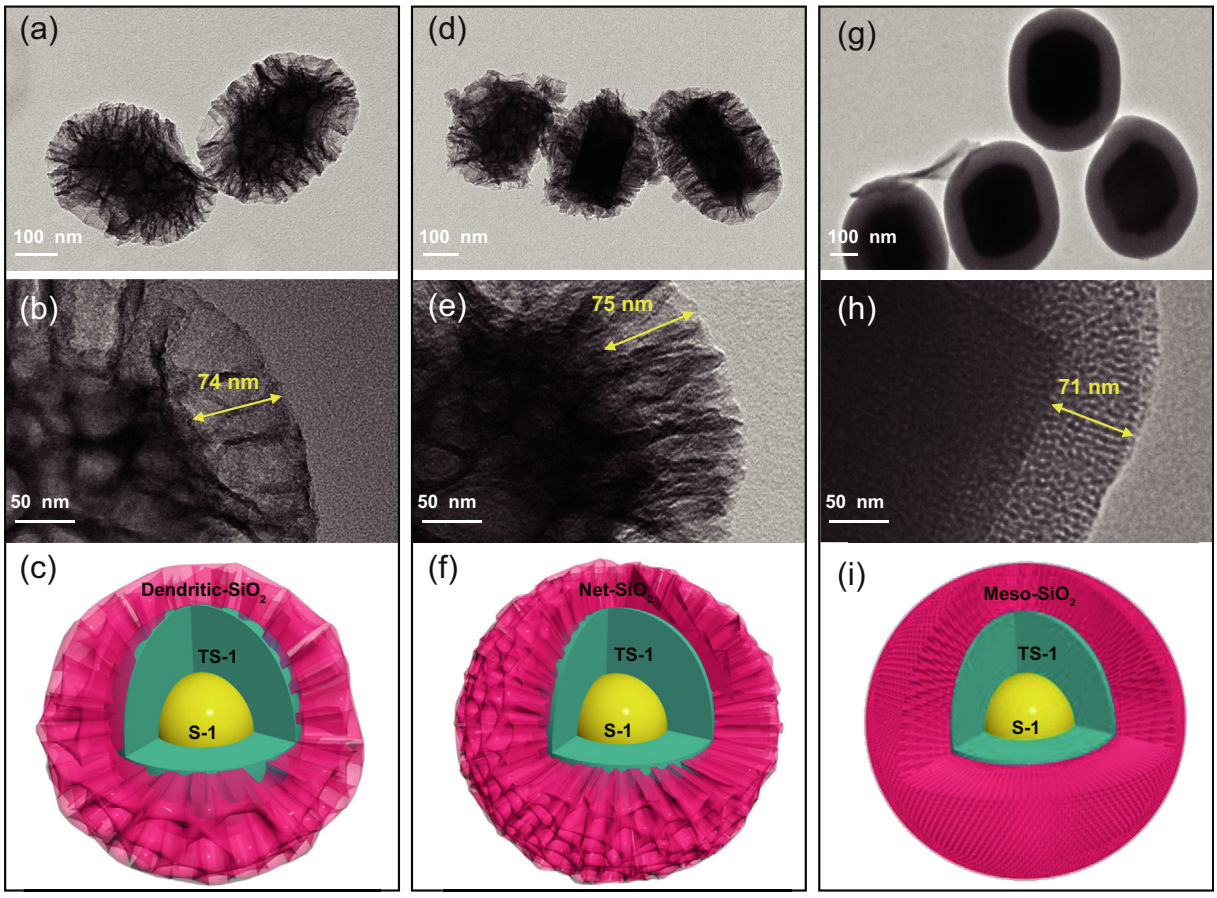

Fig. 7. TEM images of S-1/TS-1@dendritic-SiO_2 (a, b), S-1/TS-1@net-SiO_2 (d, e), S-1/TS-1@meso-SiO_2 (g, h) and schematic diagrams of S-1/TS-1@dendritic-SiO_2 (c), S-1/TS-1@net-SiO_2 (f), S-1/TS-1@meso-SiO_2 (i).

Table 1
Textural properties of S-1/TS-1, S-1/TS-1@dendritic-SiO_2, S-1/TS-1@net-SiO_2 and S-1/TS-1@meso-SiO_2.

Sample	S_{BET} (m^2g^{-1})	V_{tot} (cm^3g^{-1})	V_{mic} (cm^3g^{-1})	V_{meso} (cm^3g^{-1})
S-1/TS-1	374.558	0.236	0.122	0.114
S-1/TS-1@dendritic-SiO_2	495.144	0.361	0.101	0.260
S-1/TS-1@net-SiO_2	567.013	0.402	0.077	0.325
S-1/TS-1@meso-SiO_2	697.469	0.539	0.016	0.523

size of 28.5 and 17.0 nm appear in S-1/TS-1@dendritic-SiO_2 and S-1/TS-1@net-SiO_2 samples, respectively. Obviously, with the decrease of ether amount in the preparation process, the mesoporous pore size decreases while the specific surface area and mesoporous volume increase (Table 1). This means that the density of SiO_2 structure progressively increases with the decreases of the ether feeding amount. This result is consistent with TEM result in Fig. 7.

As shown in the NH_3-TPD spectra (Fig. 8), it is observed that all samples exhibit two NH_3 desorption peaks at 139 and 327 °C, which are attributed to weak acid centers. The intensity of the two desorption peaks diminishes with the increase of SiO_2 shell density, which means that the number of surface acid sites of the three samples follows the order:

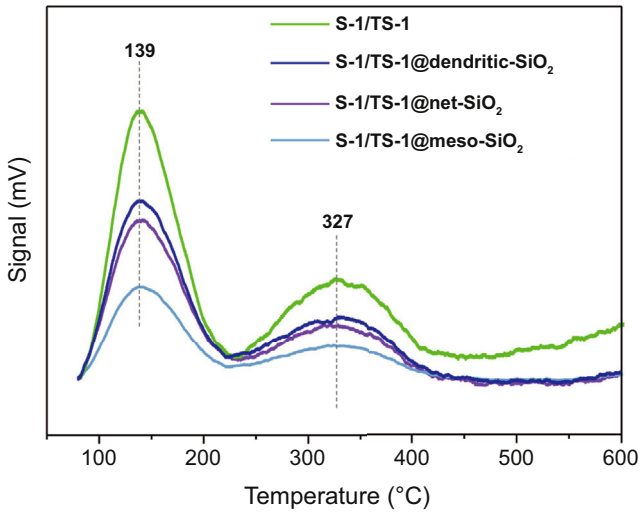

Fig. 8. NH_3-TPD spectra of S-1/TS-1, S-1/TS-1@dendritic-SiO_2, S-1/TS-1@net-SiO_2 andS-1/TS-1@meso-SiO_2.

S-1/TS-1@dendritic-SiO_2 > S-1/TS-1@net-SiO_2 > S-1/TS-1@meso-SiO_2. The acidity of the zeolites was further investigated by pyridine-IR. The pyridine-IR results in Table 2 indicated that both the Lewis acid sites and trace

Table 2
The chemical acidity data of S-1/TS-1, S-1/TS-1@dendritic-SiO_2, S-1/TS-1@net-SiO_2 and S-1/TS-1@meso-SiO_2.

Sample	Brønsted acid (μmol g^{-1})	Lewis acid (μmol g^{-1})	Total acid (μmol g^{-1})
S-1/TS-1	18.7	247.8	266.4
S-1/TS-1@dendritic-SiO_2	10.2	169.4	179.6
S-1/TS-1@net-SiO_2	6.8	154.5	161.3
S-1/TS-1@meso-SiO_2	2.3	121.5	123.8

Brønsted acid sites are contained in the samples. The Lewis and Brønsted acid amounts decrease with the increases of SiO_2 shell density, which is consistent with the NH_3-TPD result.

Furthermore, the propene epoxidation performance of the Au/S-1/TS-1@dendritic-SiO_2, Au/S-1/TS-1@net-SiO_2 and Au/S-1/TS-1@meso-SiO_2 catalysts with the similar Au loading (ca. 0.10 wt %) are shown in Fig. 9. The Au/S-1/TS-1@meso-SiO_2 catalyst with the densest SiO_2 shell shows the highest PO selectivity of 96.1%, compared to that of Au/S-1/TS-1@net-SiO_2 (94.6%) and Au/S-1/TS-1@dendritic-SiO_2 (93.9%). An obvious trend can be inferred that the PO selectivity of the catalyst benefits from the decrease of the amount of exposed Lewis and Brønsted acid sites by coating denser SiO_2 shell. The reason for the unique PO selectivity is that the dendritic SiO_2 shell with fantastic dendritic structure preferentially grows on the defective Ti–OH acid sites with lower energy barrier, thus reducing the occurrence of side reactions.

Although Lewis acid sites on the surface of S-1/TS-1 may cause side reactions, they are closely related to the active Au–Ti centers. It is known that both the close site $Ti(OSi)_4$ species and the open site $Ti(OSi)_3OH$ species are active for epoxidation by forming the Ti–OOH intermediate [44–49]. Fig. 9a shows the C_3H_6 conversion of the three catalysts. It's worth noting that Au/S-1/TS-1@dendritic-SiO_2 affords an appropriate C_3H_6 conversion of 4.18%. This is because dendritic-SiO_2 with lower shell density maintains enough active sites on the surface to guarantee the C_3H_6 conversion. In contrast, the C_3H_6 conversion of Au/S-1/TS-1@meso-SiO_2 sharply decreased to 2.31%. This is because overmuch SiO_2 shell will shield more active sites, resulting in insufficient Ti active sites to form Ti–OOH intermediate. With the further increase of SiO_2 shell density, the effective Ti active sites are gradually covered, leading to further decrease of C_3H_6 conversion. As the SiO_2 shell becomes a denser meso-SiO_2 structure, both acidic and non-acidic Ti active sites are extensively covered, resulting in a significant decline in C_3H_6 conversion.

In addition, with the increase of SiO_2 shell density, a volcanic-shape relationship between the shell density and PO formation rate was emerged in Fig. 9b. It is found that Au/S-1/TS-1@dendritic-SiO_2 shows the highest PO formation rate. This result is attributed to the unique shaggy SiO_2 shell structure. The shaggy dendritic SiO_2 shell not only covers part of the defect $Ti(OSi)_3OH$ sites that provide acidity, but

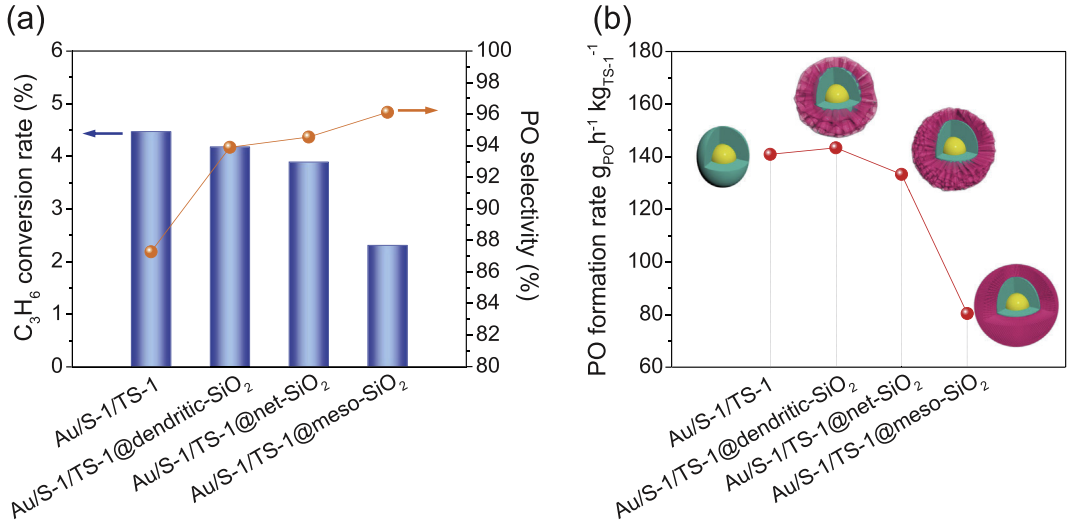

Fig. 9. The catalytic performance of Au/S-1/TS-1, Au/S-1/TS-1@dendritic-SiO_2, Au/S-1/TS-1@net-SiO_2 and Au/S-1/TS-1@meso-SiO_2.

also retains enough active sites on the surface. Therefore, moderate regulation of the number of acid sites will be of great importance to the design of catalysts with high PO selectivity and H_2 efficient for direct propene epoxidation with H_2 and O_2.

4. Conclusions

In summary, an efficient S-1/TS-1@dendritic-SiO_2 support with three-layer core–shell structure was developed. The as-synthesized Au/S-1/TS-1@dendritic-SiO_2 catalyst showed fantastic PO selectivity of 93.9% and stable PO formation rate of 143.4 $g_{PO}h^{-1}kg_{TS\text{-}1}^{-1}$. It is found that the middle layer of TS-1 (only 90 nm) can provide great mass transfer ability. This could be responsible for the excellent stability. Moreover, an inert SiO_2 shell can cover part of the Lewis and Brønsted acid sites provided by defective Ti–OH, which could improve the selectivity by inhibiting the PO ring–opening reactions. In addition, with the increase of SiO_2 shell density, the volcanic-shape relationship between the shell density and PO formation rate was emerged. It is found that overmuch SiO_2 shell will shield a large number of active sites, resulting in a sharp decrease in C_3H_6 conversion. Due to the unique shaggy dendritic SiO_2 shell structure of Au/S-1/TS-1@dendritic-SiO_2, it not only covers part of the defective Ti–OH sites that provide acidity, but also retains enough active sites on the surface. This study will be of great importance to the design and synthesis of highly efficient supported zeolite catalysts for direct propene epoxidation with H_2 and O_2.

Conflict of interest

There is no conflict of interest.

Acknowledgements

This work was supported by the Natural Science Foundation of China (21978325, 21776312, 22078364) and Postgraduate Innovation Engineering (YCX2020044).

Appendix A. Supplementary data

Supplementary data to this article can be found online at https://doi.org/10.1016/j.gee.2020.11.017.

References

[1] M. Schömer, C. Schüll, H. Frey, J. Polym. Sci., Polym. Chem. Ed. 51 (2013) 995–1019.
[2] J. Huang, T. Takei, T. Akita, H. Ohashi, M. Haruta, Appl. Catal., B 95 (2010) 430–438.
[3] T.A. Nijhuis, M. Makkee, J.A. Moulijn, B.M. Weckhuysen, Ind. Eng. Chem. Res. 45 (2006) 3447–3459.
[4] V. Russo, R. Tesser, E. Santacesaria, M.D. Serio, Ind. Eng. Chem. Res. 52 (2013) 1168–1178.
[5] S. Bordiga, A. Damin, F. Bonino, G. Ricchiardi, C. Lamberti, A. Zecchina, Angew. Chem. Int. Ed. 41 (2002) 4734–4737.
[6] S.J. Khatib, S.T. Oyama, Catal. Rev. 57 (2015) 306–344.
[7] M. Akimoto, K. Ichikawa, E. Echigoya, J. Catal. 76 (1982) 333–344.
[8] M. Haruta, B.S. Uphade, S.A. Tsubota, A. Miyamoto, Res. Chem. Intermed. 24 (1998) 329–336.
[9] O.P.H. Vaughan, G. Kyriakou, N. Macleod, M. Tikhov, R.M. Lambert, J. Catal. 236 (2005) 401–404.
[10] H. Yang, D. Tang, X. Lu, Y. Yuan, J. Phys. Chem. C 113 (2009) 8186–8193.
[11] B.S. Uphade, Y. Yamada, T. Akita, T. Nakamura, M. Haruta, Appl. Catal. A-Gen. 215 (2001) 137–148.
[12] J. Lu, X. Zhang, J.J. Bravo-Suárez, K.K. Bando, T. Fujitani, S.T. Oyama, J. Catal. 250 (2007) 350–359.
[13] N. Yap, R.P. Andres, W.N. Delgass, J. Catal. 226 (2004) 156–170.
[14] T.A. Nijhuis, B.J. Huizinga, M. Makkee, J.A. Moulijn, Ind. Eng. Chem. Res. 38 (1999) 884–891.
[15] X. Feng, Y.B. Liu, Y.C. Li, C.H. Yang, Z.H. Zhang, X.Z. Duan, X.G. Zhou, AIChE J. 62 (2016) 3963–3972.
[16] G.W. Zhan, M.M. Du, D.H. Sun, J.L. Huang, X. Yang, Ind. Eng. Chem. Res. 50 (2011) 9019–9026.
[17] M. Du, G. Zhan, Y. Xin, H. Wang, W. Lin, Z. Yao, Z. Jing, L. Ling, J. Huang, D. Sun, J. Catal. 283 (2011) 192–201.
[18] T. Ishida, M. Nagaoka, T. Akita, M. Haruta, Chem. Eur J. 14 (2008) 8456–8460.
[19] L. Xu, Y. Ren, H. Wu, Y. Liu, Z. Wang, Y. Zhang, J. Xu, H. Peng, P. Wu, J. Mater. Chem. 21 (2011) 10852.
[20] X. Feng, X. Duan, G. Qian, X. Zhou, D. Chen, W. Yuan, Appl. Catal., B 150 (2014) 396–401.
[21] X. Feng, N. Sheng, Y.B. Liu, X.B. Chen, X.G. Zhou, ACS Catal. 7 (2017) 266–2675.
[22] N. Sheng, Z. Liu, Z. Song, D. Lin, X. Feng, Y. Liu, X. Chen, D. Chen, X. Zhou, C. Yang, Chem. Eng. J. 377 (2018) 119954.
[23] X. Feng, X. Duan, H. Cheng, G. Qian, D. Chen, W. Yuan, X. Zhou, J. Catal. 325 (2015) 128–135.
[24] S. Kanungo, K.S. Keshri, A.J.F. Van Hoof, M.F.N. D'Angelo, J.C. Schouten, T.A. Nijhuis, E.J.M. Hensen, B. Chowdhury, J. Catal. 344 (2016) 434–444.
[25] Z.N. Song, X. Feng, N. Sheng, D. Lin, Y.C. Li, Y.B. Liu, X.B. Chen, D. Chen, X.G. Zhou, C.H. Yang, Chem. Eng. J. 377 (2018) 119927.
[26] C.S. Cundy, J.O. Forrest, R.J. Plaisted, Microporous Mesoporous Mater. 66 (2003) 143–156.
[27] R.B. Khomane, B.D. Kulkarni, A. Paraskar, S.R. Sainkar, Mater. Chem. Phys. 76 (2002) 99–103.
[28] X. Feng, X. Duan, J. Yang, G. Qian, X. Zhou, D. Chen, W. Yuan, Chem. Eng. J. 278 (2015) 234–239.
[29] T. Guo, B. Wang, X. Peng, M. Lin, B. Zhu, Y. Zhang, C. Xia, W.L. Liao, X. Shu, Ind. Eng. Chem. Res. 58 (2019) 7892–7899.
[30] Z.N. Song, X. Feng, N. Sheng, D. Lin, Catal. Today 347 (2020) 102–109.
[31] C. Shen, Y.J. Wang, J.H. Xu, G.S. Luo, Chem. Eng. J. 259 (2015) 552–561.
[32] X. Feng, X. Duan, G. Qian, X. Zhou, D. Chen, W. Yuan, J. Catal. 317 (2014) 99–104.
[33] X. Feng, Z. Song, Y. Liu, X. Chen, X. Jin, W. Yan, C. Yang, J. Luo, X. Zhou, D. Chen, ACS Catal. 8 (2018) 10649–10657.
[34] X. Feng, J. Yang, X. Duan, Y. Cao, B. Chen, W. Chen, D. Lin, G. Qian, D. Chen, C. Yang, ACS Catal. 8 (2018) 7799–7808.
[35] W. Lee, L. Lai, M. Akatay, E. Stach, F. Ribeiro, W. Delgass, J. Catal. 296 (2012) 31–42.
[36] Q. Guo, K. Sun, P.Z. Feng, G. Li, M. Guo, F. Fan, P.C. Li, Chem. Eur J. 18 (2012) 13854–13860.
[37] J. Su, G. Xiong, J. Zhou, W. Liu, D. Zhou, G. Wang, X. Wang, H. Guo, J. Catal. 288 (2012) 1–7.
[38] Z. Li, W. Ma, Q. Zhong, Ind. Eng. Chem. Res. 58 (2019) 4010–4016.
[39] Z. Zhang, X. Zhao, G. Wang, J. Xu, M. Lu, Y. Tang, W. Fu, X. Duan, G. Qian, D. Chen, X. Zhou, AIChE J. 66 (2020) e16815.

[40] A. Corma, H. García, Chem. Rev. 102 (2002) 3837–3892.
[41] L. Wu, Z. Tang, Y. Yu, X. Yao, W. Liu, Chem. Commun. 54 (2018) 6384–6387.
[42] Y. Yu, Z. Tang, W. Liu, J. Wang, Z. Chen, K. Shen, R. Wang, H. Liu, X. Huang, Y. Liu, Appl. Catal. A-Gen. 587 (2019) 117270.
[43] X. Du, J. He, Langmuir 27 (2011) 2972–2979.
[44] D.H. W Jr., W.N. Delgass, K.T. Thomson, J. Am. Chem. Soc. 126 (2004) 2956–2962.
[45] L. Wu, S. Zhao, L. Lin, X. Fang, Y. Liu, M. He, J. Catal. 337 (2016) 248–259.
[46] M.G. Clerici, Kinet. Catal. 56 (2015) 450–455.
[47] X. Nie, X. Ji, Y. Chen, X. Guo, C. Song, Mol. Catal. 441 (2017) 150–167.
[48] Z. Song, X. Feng, Y. Liu, C. Yang, X. Zhou, Prog. Chem. 28 (2016) 1762–1773.
[49] B. Chowdhury, J.J. Bravo-Suárez, M. Daté, S. Tsubota, M. Haruta, Angew. Chem. Int. Ed. 45 (2006) 412–415.